J Mater Sci: Mater Electron (2014) 25:1466–1473
DOI 10.1007/s10854-014-1753-1

Vortex pinning and magnetic peak effect in $Eu(Eu,Ba)_{2.125}Cu_3O_x$

E. Altin · D. M. Gokhfeld · S. Demirel · E. Oz · F. Kurt · S. Altin · M. E. Yakinci

Received: 30 October 2013 / Accepted: 20 January 2014 / Published online: 25 January 2014

Abstract Eu–Ba–Cu–O composition was synthesized by solid state reaction technique. To determine optimum growth temperature, heat treatment was examined on the material at 880–1,100 °C. Microstructural evolution, phase formation and elemental distribution depending on heat treatments were examined by using X-ray diffraction, scanning electron microscope, energy dispersive X-ray spectroscope analysis. Optimum fabrication conditions were determined as 1,020 °C for 24 h under oxygen atmosphere and detailed characterization of corresponding compound was performed. The magnetization hysteresis loops are expounded to be the product of superconducting Eu-123 grains and magnetic Eu^{2+} ions. The peak effect on the magnetization curves was described by the extended critical state model. Scaling of the pinning force was found such that the peak position is proportional to the irreversibility field H_{irr} and the maximum pinning force is proportional to H_{irr}^2.

E. Altin · S. Demirel · E. Oz · F. Kurt
Bilimsel ve Teknolojik Araştırma Merkezi, Inonu Universitesi, 44280 Malatya, Turkey

D. M. Gokhfeld (✉)
L.V. Kirensky Institute of Physics SB RAS, 660036 Krasnoyarsk, Russia
e-mail: gokhfeld@iph.krasn.ru

S. Altin · M. E. Yakinci
Fen Edebiyat Fakultesi, Fizik Bolumu, Superiletkenlik Arastirma Grubu, Inonu Universitesi, 44280 Malatya, Turkey

1 Introduction

After discovery Y–Ba–Cu–O materials in 1987 [1], many efforts were devoted to improve superconducting transition temperature T_c and current carrying capacity. There are three different phases on YBCO family as Y-123, Y-124 and Y-247 and the superconducting transition temperatures were obtained at about 90, 80 and 80 K respectively [2–5]. The main importance of the YBCO family is high current carrying capacity at the liquid nitrogen temperature and simple fabrication compared with Bi- or Tl-based high-T_c superconductors [6, 7].

Rare earth elements (Re = Nd, Eu, Sm, etc.) were substituted/doped into the Y site to increase T_c and also the critical current density J_c [8–11]. While the T_c value of the Re-123 system remained almost unchanged in the range of ~92–96 K compared to the Y-123 system, it was found that the J_c value increased from 10^4 A/cm^2 for the Y-123 system to 10^6 A/cm^2 for the Re-123 system. The Re-123 materials contain defects such as dislocations, impurities, stacking faults, point defects, grain boundaries, which improve the magnetic flux pinning in the superconducting state and the J_c value of the system. This feature of the Re-123 system makes it a suitable candidate for technological applications such as cables, magnets, etc. [12].

Fishtail or magnetic peak effect is frequently observed on the hysteretic magnetization of Re-123 systems. The magnetic peak effect, when the magnetic moment increases with increasing applied field, is one of the important subject for high magnetic fields applications [13]. Its origin is not clear and one of the models is based on the dynamic flux transition from collective creep to plastic creep or the other is a thermodynamic vortex phase transition from an ordered vortex glass to an entangled vortex glass [14]. In melt processed superconductors, the peak position and the

magnetization amplitude could be modified by processing. It is found that the peak effect depends on the defect structure in the sample [15].

In presented work we investigated $Eu(Eu,Ba)_{2.125}Cu_3O_x$ composition synthesized by solid state reaction technique. Heat treatment was examined on the material at 880–1,100 °C for 24 h. Microstructure and phase evolution on the samples was investigated by X-ray diffraction (XRD), scanning electron microscope (SEM) and energy dispersive X-ray spectroscope (EDX) analysis. Electrical and magnetic properties were investigated that allows selecting the optimal heat treatment conditions. Magnetization of the sample heat treated at 1,020 °C was investigated in detail. The extended critical state model was applied to fit and parameterize the hysteretic magnetization loops with the peak effect.

2 Experimental details

The samples were prepared using solid state reaction technique. High purity powders of Eu_2O_3, $BaCO_3$ and CuO were weighed in the appropriate amounts to give nominal composition of $Eu(Eu,Ba)_{2.125}Cu_3O_x$. The powders were mixed using an agate mortar and then sintered at 900 °C for 24 h with intermediate grinding and mixing. After sintering, the powders were pressed into pellets by load of 4 t. The pellets were heat treated at temperatures between 880 and 1,100 °C for 24 h under oxygen atmosphere. Heating and cooling rates were chosen as 10 °C/min. The sample heat treated at 1,100 °C had nonstochiometric formation and it has stuck to the alumina crucible after the heat treatment cycle.

The structural characterization of the materials was investigated by XRD. Scan speed was selected as 2° min^{-1} in the range of $2\theta = 30°–80°$. Automated Rigaku RadB Dmax X-ray diffractometer with CuK_α radiation was used for the XRD analysis. Calculations of crystallite size and strain were performed using XRD pattern.

The microstructural and compositional characterization of the materials was performed with Leo EVO-40 XVP SEM and BRUKER X-flash detector 4010 EDX.

Temperature dependence of resistivity ($\rho-T$) of the samples fabricated was carried out by closed cycle Leybold LT-10 cryostat system combined with SRS ac bridge system using 17.7 Hz frequency. For resistivity measurements, the four probe electrical contacts were performed by silver paste. The cooling rate was 1.5 K/min for all the samples. The T_c values of samples were determined by the resistivity differentiation $d\rho(T)/dT$ as the peak temperature on the $d\rho(T)/dT$ plot. Magnetization measurements (temperature dependence $M–T$ and hysteretic loops $M–H$ at $T = 10$, 20, 30, 40 and 50 K) were performed using Quantum Design PPMS system up to 9 T. The critical current density was calculated using the Bean model. The pinning force was calculated from $M–H$ measurements.

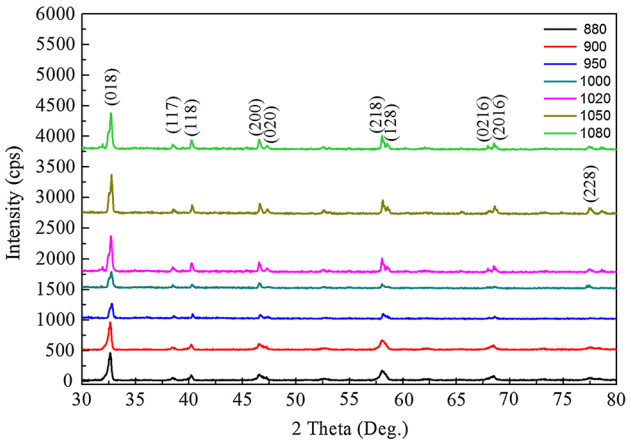

Fig. 1 XRD patterns of the Eu-based system prepared under different heat treatment conditions

3 Results and discussion

3.1 XRD analysis

XRD patterns of the samples heat treated at different temperatures are shown in Fig. 1. All the peaks in the XRD patterns were assigned to $EuBa_2Cu_3O_{6+x}$ phase without any impurity phases. After the Rietveld refinement of the XRD data, it was determined that the samples showed orthorhombic symmetry. The calculated unit cell parameters, depending on the heat treatment conditions, are given in Table 1. It was found that the unit cell parameters are the same as the parameters of the Eu-123 system [16]. The results clearly indicated that the Eu-123 phase was obtained.

Crystallite size and lattice strain due to imperfections, impurities and dislocations can be found from the XRD peak broadening. The crystallite size D was calculated by using the Scherrer equation [17]:

$$D = \frac{k\lambda}{\beta_c \cos\theta} \quad (1)$$

where λ is the wavelength of the X-ray ($\lambda_{CuK\alpha}$= 1.54056 Å), k is a constant as 0.94, β_c is the peak width at half maximum intensity and θ is the XRD peak position. The calculated average crystallite sizes were given in Fig. 2. The smallest crystallite size as 40 nm was found in the sample heat treated at 1,020 °C. The specific surface area and the Gibbs free energy increase with lowering the average crystallite size. The increase of the crystallite size after the minima is related to the nonstochiometric crystallite formation.

Table 1 Lattice parameters and EDX data of the samples fabricated at different heat treatment cycles

Heat temp. (°C)	*a* (Å)	*b* (Å)	*c* (Å)	Lattice volume (Å^3)	% Eu	% Ba	% Cu
880	3.895 ± 0.02	3.850 ± 0.02	10.322 ± 0.04	154.79	22.09 ± 1.0	28.78 ± 1.1	49.13 ± 0.9
900	3.891 ± 0.03	3.843 ± 0.02	10.300 ± 0.03	154.02	21.36 ± 0.9	27.51 ± 1.0	51.13 ± 0.9
950	3.898 ± 0.02	3.889 ± 0.03	10.230 ± 0.04	155.07	15.41 ± 1.9	33.54 ± 2.0	51.06 ± 0.8
1,000	3.908 ± 0.03	3.873 ± 0.02	10.229 ± 0.03	154.82	15.8 ± 2.0	33.66 ± 2.0	50.54 ± 0.9
1,020	3.909 ± 0.02	3.845 ± 0.03	10.314 ± 0.04	155.02	21.18 ± 1.0	28.43 ± 1.3	50.39 ± 0.8
1,050	3.930 ± 0.03	3.841 ± 0.02	10.258 ± 0.03	155.84	20.95 ± 1.0	28.01 ± 1.0	51.04 ± 0.9
1,080	3.942 ± 0.03	3.832 ± 0.03	10.222 ± 0.02	154.41	20.87 ± 1.0	28.17 ± 1.0	50.96 ± 0.8
1,100	Partially melted during heat treatment						

Theoretical elemental distribution for $Eu(Eu,Ba)_{2.125}Cu_3O_x$ composition: Eu: 20 %, Ba: 32 %, Cu: 48 %, and for the pure Eu-123 phase: Eu: 16.7 %, Ba: 33.3 %, Cu: 50 %

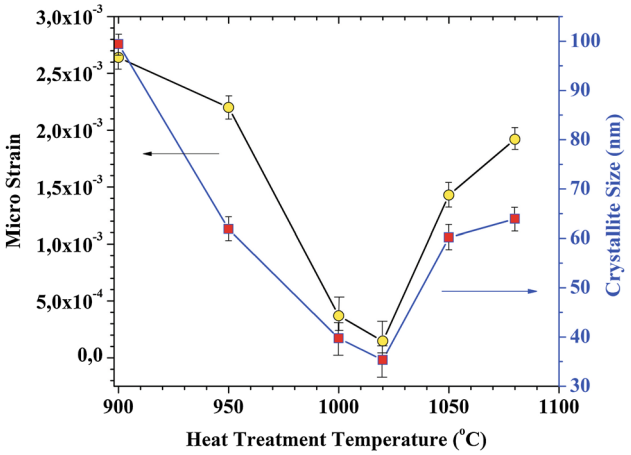

Fig. 2 Strain field and averaged crystallite size of the Eu-123 samples as a function of heat treatment temperature

The Williamson–Hall method [18] can be used for analysis of a strain in the samples. The peak broadening on the XRD can be given by $\beta_{hkl} = \beta_c + \beta_s$, where β_{hkl} is the full width at half the maximum of the XRD peak, β_c is the crystallite size contribution and $\beta_s = 4\varepsilon tan\ \theta$ is the strain induced broadening with the microstrain ε. The crystallite size contribution on β_{hkl} is calculated by using the Scherrer Eq. (1). It is convenient to write the combined equation as below:

$$\beta_{hkl}\cos\theta_{hkl} = \frac{k\lambda}{D} + 4\varepsilon\sin\theta \qquad (2)$$

The strain ε was calculated from the slope of the dependence $\beta_{hkl}\cos\theta_{hkl}$ on $4sin\ \theta$ (see results on Fig. 2). The lattice strain has the lowest value ($<10^{-4}$) for the sample heat treated at 1,020 °C which indicated the optimum heat treatment temperature of the sample. The strain below and above 1,020 °C is related to diffusion of atoms which can cause an increase of lattice dimensions.

3.2 Microstructural analysis

The surface morphology of the samples obtained is shown in Fig. 3a–g. According to EDX data, the atomic concentration in the samples is presented in Table 1. As seen in Fig. 3a–c, the grain size in the samples prepared at 880–950 °C changed in the range between 1 and 5 μm and some porosity was observed on the surface of the samples. When the heat treatment temperature was increased above 950 °C, the compacted and large grains with size of 5–20 μm were formed on the sample (Fig. 3d–g). For such heat treatment the porosity on the surface of the samples disappeared. It should be noted that the grains formed between 1,000 and 1,080 °C were in the cubic form and tightly connected. These tightly connected grains are very important for transport properties of the samples because the charge carriers participating to the transport phenomena undergoes a minimum scattering on the large grains and so the resistivity of the samples reduces. The sample fabricated at 1,100 °C has layered crystallite formation but the grain connection is poor and so the sample is not superconducting as seen in the electrical properties section. EDX analysis of the samples demonstrates (Table 1) that the elemental ratios of the sample which heat treated at 1,020 °C are very close to the theoretical calculation. The deviation of the elemental ratio with heat treatment is related to the structural formation, evaporations, etc.

3.3 Electrical properties

Temperature dependence of the resistivity of the samples prepared by different heat treatments is shown in Fig. 4a. The sample prepared at 880 °C exhibited highest normal state resistance, which can be attributed to porosities on the sample surface and weak-connection among the grains due to insufficient heat treatment (see Fig. 2a). The temperature T_0 at which dissipation appears and T_c of the sample

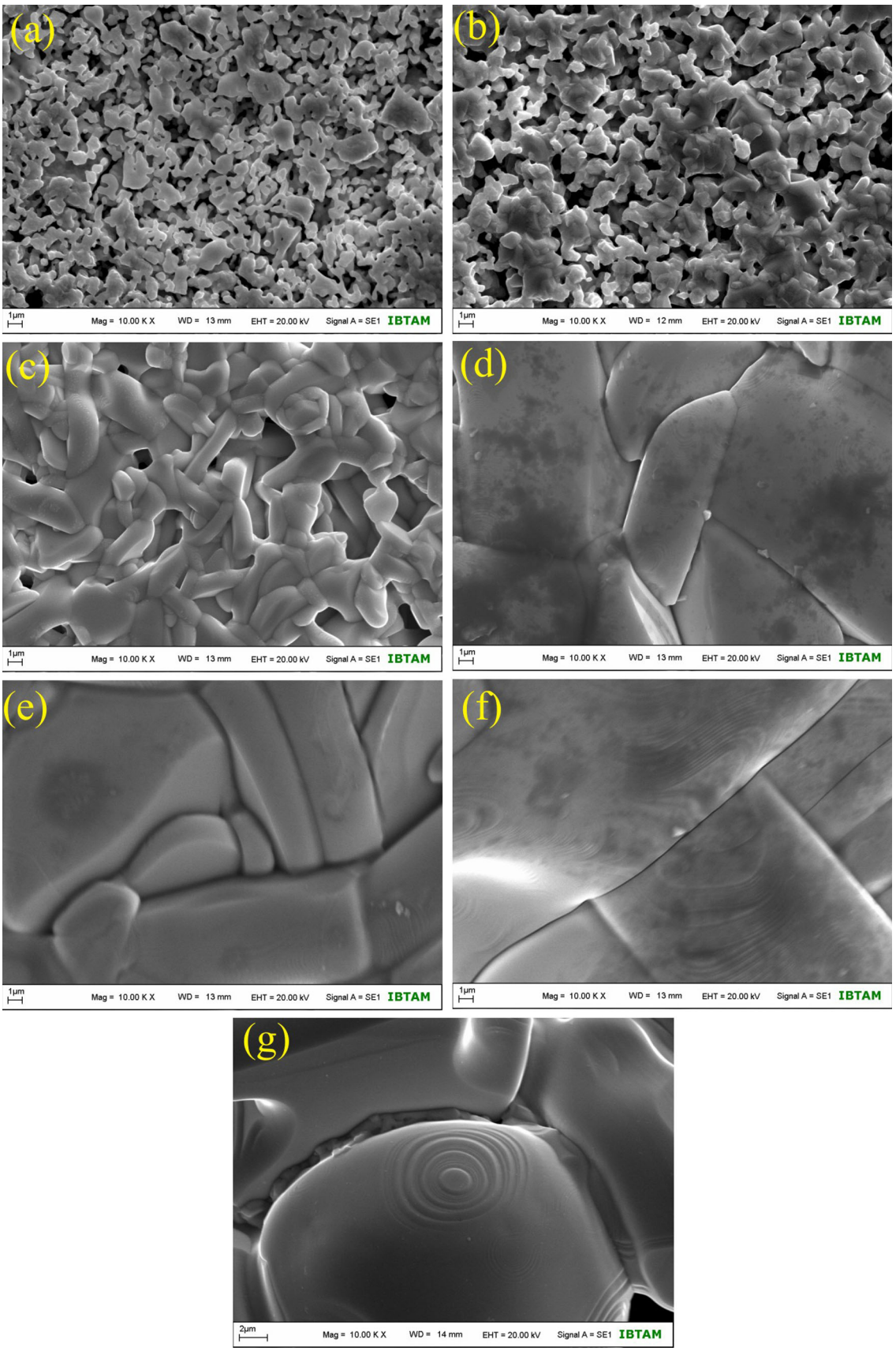
(a)
1μm Mag = 10.00 K X WD = 13 mm EHT = 20.00 kV Signal A = SE1 IBTAM
(b)
1μm Mag = 10.00 K X WD = 12 mm EHT = 20.00 kV Signal A = SE1 IBTAM
(c)
1μm Mag = 10.00 K X WD = 13 mm EHT = 20.00 kV Signal A = SE1 IBTAM
(d)
1μm Mag = 10.00 K X WD = 13 mm EHT = 20.00 kV Signal A = SE1 IBTAM
(e)
1μm Mag = 10.00 K X WD = 13 mm EHT = 20.00 kV Signal A = SE1 IBTAM
(f)
1μm Mag = 10.00 K X WD = 13 mm EHT = 20.00 kV Signal A = SE1 IBTAM
(g)
2μm Mag = 10.00 K X WD = 14 mm EHT = 20.00 kV Signal A = SE1 IBTAM

◀**Fig. 3** SEM photographs of the samples prepared at **a** 880 °C, **b** 900 °C, **c** 950 °C, **d** 1,000 °C, **e** 1,020 °C, **f** 1,050 °C and **g** 1,080 °C

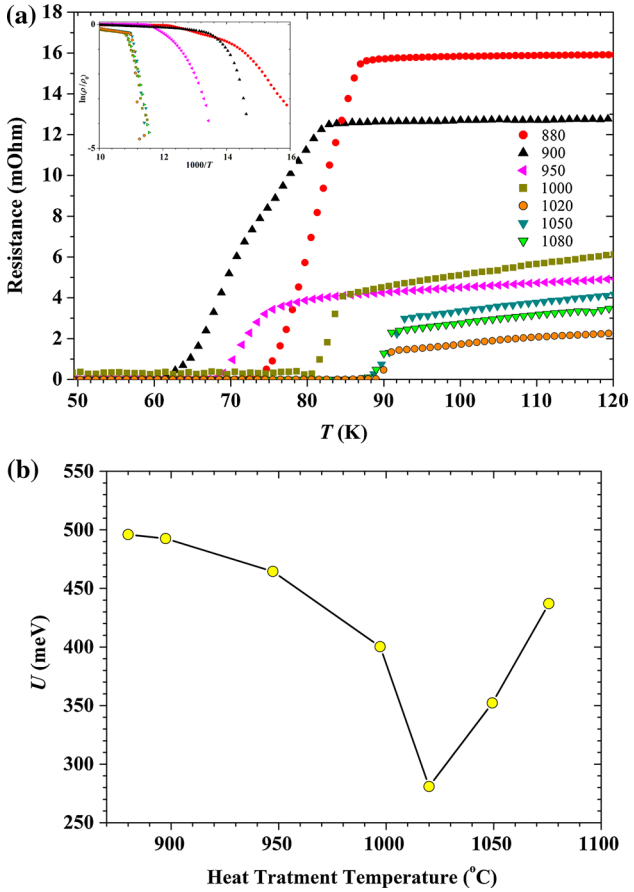

Fig. 4 Electrical properties of the samples prepared at different heat treatment temperatures. Temperature dependence of resistance **(a)** and temperature dependence of the Arrhenius pinning potential **(b)**. *Inset* on **a** demonstrates

Table 2 Superconducting properties and the room temperature resistance of the samples fabricated at different heat treatment cycles

Heat temp. (°C)	T_c (K)	T_0 (K)	ΔT (K)	R_{room} (mΩ)
880	87.53	74.27	13.26	17
900	83.25	62.25	21	14
950	75.65	68.47	7.18	9.7
1,000	84.63	79.62	5.01	12
1,020	93.47	89.53	4.17	5.2
1,050	92.77	87.63	5.14	8.7
1,080	91.81	88.47	5.34	9.3

prepared at 880 °C are equal to 62–88 K, respectively. When the heat treatment temperature was increased, it was observed that the normal state resistance at the room temperature (R_{room}) reduced and the T_c and T_0 values of the samples increased (Table 2). The best T_c and T_0 values were obtained for the sample prepared at 1,020 °C.

When we consider the electrical resistance results together with the surface morphologies, it is seen that the samples which have large and tightly connected grains showed higher T_c and T_0 values. Samples heat treated at low temperatures showed zero resistance at lower temperatures, which can be attributed to a large number of grain boundaries and porosities in these samples. This is a result of scattering of the charge carriers on grain boundaries, as mentioned in the SEM analysis. So the lowest room temperature resistance value was obtained in the sample heat treated at 1,020 °C.

The activation energy U plays an important role for determination of the flux dynamics in high-T_c materials. U also reveals the height of energy barriers of the high-T_c materials which control the vortex motion in the vortex liquid [19]. In the thermally activated flux flow (TAFF) region, the thermally activated resistivity is defined by the Arrhenius equation:

$$\rho = \rho_0 e^{\left(-\frac{U(J,H,T)}{k_B T}\right)}, \tag{3}$$

where ρ_0 is the pre-exponent factor, k_B is the Boltzmann constant and U is the activation energy for the flux motion which depends on the temperature T, the current density J, and the applied magnetic fields H. At constant current, the functional dependence of $U(H)$, can be calculated from the slope of $\ln(\rho/\rho_0)$ versus $1/T$ as shown on inset in Fig. 4a.

It should be mentioned that the decrease of the activation energy promotes the thermally activated dissipation due to the vortex motion in a single-crystal sample. For a polycrystalline superconductor dissipation begins in intergrain boundaries. So the U values determined from the Arrhenius equation are related to transparency of the intergrain boundaries in the samples.

The activation energy values calculated from Eq. (5) are given in Fig. 4b. The U values were changed with heat treatment temperature. The lowest activation energy is obtained for the sample heat treated at 1,020 °C that shows the transparent intergrain boundaries.

3.4 Magnetic properties

We have investigated the sample heat treated at 1,020 °C which has high quality crystal formation and highest T_c value among the sample. Figure 5 shows magnetization hysteresis loops of the sample at 10–80 K. The hysteresis loops are tilted in the anticlockwise direction. The measured M–H curves are the superposition of a hysteresis loop $M_S(H)$ of the superconducting crystallites and a paramagnetic magnetization curve $M_P(H)$ such that the full

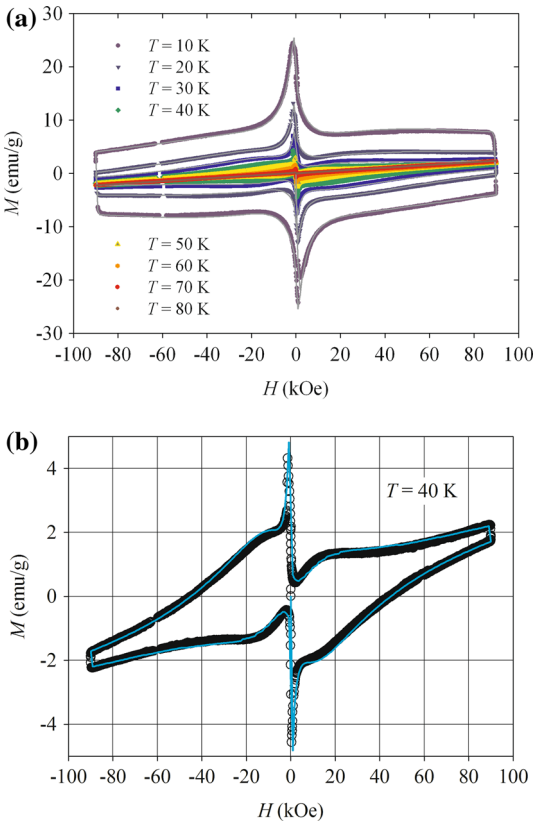

Fig. 5 Hysteretic magnetization curves of the sample heat treated at 1,020 °C, T = 10–80 K **(a)** and T = 40 K **(b)**. *Solid lines* are ECSM curves

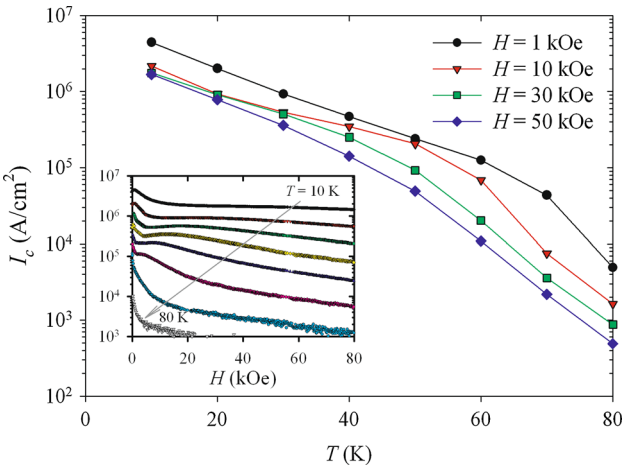

Fig. 6 Temperature dependence of the critical current density of the sample heat treated at 1,020 °C. *Lines* are a guide for eyes. *Inset* demonstrates $I_c(H)$ dependence of the same sample at different temperatures (10–80 K)

hysteretic loop $M(H) = M_S(H) + M_P(H)$. The noticeable paramagnetic contribution is surprising because Eu^{3+} ions in Eu-123 have the local magnetic moment equal to zero. However Eu^{3+} may be reduced to Eu^{2+} during high-temperature solid state reaction and Eu^{2+} ions substitute for Ba^{2+} in Eu-123 [20]. The magnetic Eu^{2+} ions can provide the observed paramagnetic contribution. The paramagnetic magnetization is given by $M_P(H) = NgJ\mu_B\ B_J(gJ\mu_B H/(k_B T))$, where N is the number of the magnetic ions per unit volume, μ_B is the Bohr magneton, k_B is the Boltzmann constant, g is Lande's g-factor, J is the angular momentum quantum number, and B_J is the Brillouin function.

The extended critical state model [21, 22] was applied to fit the $M_S(H)$ loops. Decreasing field dependence of the local critical current density is described by.

$$j_c'(B) = \frac{j_{c0}}{\frac{|B|}{B_0} + \exp\left(\frac{|B|}{B_1}\right)}, \tag{4}$$

where j_{c0} is the local critical current density at $B = 0$, B_0 and B_1 determine the decreasing rate at different scales of magnetic fields. The peak effect is introduced by.

$$j_c(B) = j_c'(B)\left(1 + A\exp\left(-\frac{\left(\ln\frac{|B|}{B_{peak}}\right)^2}{2\left(\frac{B_w}{B_{peak}}\right)^2}\right)\right), \tag{5}$$

where B_{peak} is the peak position, B_w and A determines the peak width and the height.

Given B_{peak} equal to experimental $\mu_0 H_{peak}$ values and Eu^{2+} ion parameters (J = 7/2, g = 2) for $M_P(H)$, the hysteretic magnetization loops are successfully described for all temperatures. Solid lines on Fig. 5 are fitting curves (the curves computed for T = 10 and 40 K are showed only to not overload the figure). Successful fitting validates the used suggestions and allows to parameterize the $M_S(H)$ and $M_P(H)$ curves. The estimated magnetic ion concentration N is equal to 1.6×10^{20} cm^{-3}.

The critical current density averaged by the sample cross-section was calculated by using the Bean formula for polycrystalline superconductors:

$$I_c = 30\Delta M/d \tag{6}$$

here I_c is the critical current density in A/cm^2, ΔM is the hysteresis loop width in emu/cm^3 and d is the average grain size in cm. The d value for the sample heat treated at 1,020 °C, resulted by both the microstructural analysis and ECSM fitting [23], is equal to 8 μm. The resulted I_c values at different T and H are plotted on Fig. 6. The critical state model is valid for applied fields larger than the first critical field of superconductor so the presented data given at 1 kOe is some underestimated [24]. The $I_c(H)$ dependencies demonstrate the fishtail effect with a spreading peak (inset in Fig. 6). Due to this peak, the sample has a high critical current density right up to highest fields at a wide temperature range.

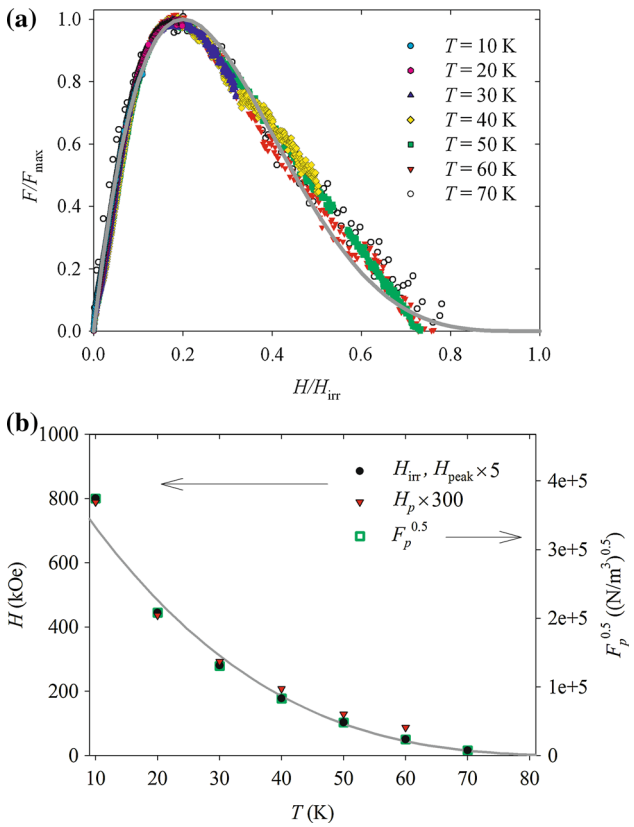

Fig. 7 Field scaling. **a** Scaling of pinning force for the sample heat treated at 1,020 °C. **b** Irreversibility field H_{irr}, peak field H_{peak} (increased in 5 times) and field of full penetration H_p (increased in 300 times) versus temperature. *Solid line* is $H(T) = 1{,}000$ kOe $\times (1-T/T_c)^3$. Also $F_{p0}^{0.5}$ is plotted to display the relation $F_{p0} \sim H_{irr}^2$

The dependence of the pinning force density on the applied magnetic field was determined from $F_p(B) = I_c(B) \times B$, here $B = \mu_0 H$. On Fig. 7a the normalized pinning force $f = F_p/F_{p0}$ is plotted as a function of the reduced field $h = H/H_{irr}$, where F_{p0} is the maximal pinning force density, H_{irr} is the irreversibility field. To define accurately H_{irr}, the $I_c(H)$ curves were decreased on the noise level. Data for $T = 80$ K are omitted on Fig. 7a due to a high noise level. We found that obtained values of F_{p0} are proportional H_{irr}^2 (Fig. 7b), so only H_{irr} was the variable parameter during scaling procedure. There is a connection between H_{irr} and the thermodynamic critical field H_c. Which is supported to be a single scaling parameter [25]. The resulted $f(h)$ curves are coincide: all points lay on the one curve and the peak of pinning is at $h = 0.2$ at all T. To fit $f(h)$ curves the scaling law [26] is applied:

$$\frac{F_p(H,T)}{F_{p0}(T)} = \frac{h^p(1-h)^q}{h_0^p(1-h_0)^q}, \qquad (7)$$

where h_0 is the position of the maximum, $h_0 = p/(p+q)$. Using the Kramer parameters ($p = 0.5$ and $q = 2$) [27] does not give good coincidence that is rather typical for high-temperature superconductors [28]. The scaled curves are fitted when $p = 1$ and $q = 4$ (solid line on Fig. 6).

Scaling of $F_p(H)$ curves is evidence of the vortex lattice transition [14, 29]. The observed temperature evolution of H_{irr} is fitted by the power function $H(T) = 1{,}000$ kOe $\times (1-T/T_c)^3$ (Fig. 7b). At all T, H_{peak} equals 0.25 H_{irr}. The fitting parameters of the extended critical state model determine the full penetration field H_p, which has the similar temperature dependence as H_{irr} and H_{peak}. The concave $H_{peak}(T)$ curve agrees with the line of the rhombohedral-to-square phase transition of the vortex lattice [30].

4 Conclusion

Microstructure and phase evolution on the Eu(Eu, Ba)$_{2.125}$Cu$_3$O$_x$ samples were investigated by XRD, SEM and EDX analysis. The lowest strain and crystallite size were obtained for the sample heat treated at 1,020 °C. The same sample has the highest T_c and lowest R_{room} among others.

Detailed investigation of magnetic characteristics was performed for the sample heat treated at 1,020 °C. Hysteresis loops were found to be superposition of the magnetization of superconducting grains and paramagnetic magnetization of the Eu^{2+} ions substituting for Ba^{2+}. Parameterization of hysteresis loops with the peak effect was performed by the extended critical state model. Correlated behavior of H_{irr} and H_{peak} and scaling of $F_p(H)$ curves with the single scale parameter H_{irr} sustain that the peak effect is caused by the vortex lattice transition.

The sample heat treated at 1,020 °C has the best superconducting properties in the investigated series. In addition the second peak arisen on the hysteretic loops retards the decrease of critical current. Thus the optimum heated Eu(Eu,Ba)$_{2.125}$Cu$_3$O$_x$ material is promising for electronic application.

References

1. K. Wu, J.R. Ashburn, C.J. Torng, P.H. Hor, R.L. Meng, L. Gao, Z.J. Huang, Y.Q. Wang, C.W. Chu, Phys. Rev. Lett. **58**, 908 (1987)
2. R.J. Cava, J.J. Krajewski, W.F. Peck Jr, B. Battelog, L.W. Rupp Jr, R.M. Fleming, A.C.W.P. James, P. Marsh, Nature **336**, 660 (1988)
3. M. Kato, M. Nakanishi, T. Miyano, T. Shimizi, M. Kakihana, K. Kosuge, J. Solid State Chem. **139**, 266 (1998)
4. F. Abbattista, M. Vallino, D. Mazza Mat, Chem. Phys. **21**, 521 (1989)

5. J.-Y. Genoud, T. Graf, G. Triscone, A. Junod, J. Muller, Phys. C **192**, 137 (1992)
6. J.Y. Juang, M.C. Hsieh, C.W. Luo, T.M. Uen, K.H. Wu, Y.S. Gou, Phys. C **329**, 45 (2000)
7. M.P. Oomen, M. Leghissa, B. Utz, H.W. Neumuller, Mater. Res. Soc. Symp. Proc. **3**, 137 (2004)
8. X. Song, Z. Chen, S. Kim, D.M. Feldmann, D. Larbalestier, J. Reeves, Y. Xie, V. Selvamanickam, Appl. Phys. Lett. **88**, 212508 (2006)
9. W.G. Suharta, S. Suasmoro, S. Pratapa, Darminto, AIP conference proceedings. **1555**, 62 (2013)
10. P.N. Barnes, J.W. Kell, B.C. Harrison, T.J. Haugan, C.V. Varanasi, M. Rane, F. Ramos, Appl. Phys. Lett. **89**, 012503 (2006)
11. M.I. Petrov, Yu.S. Gokhfeld, D.A. Balaev, S.I. Popkov, A.A. Dubrovskiy, D.M. Gokhfeld, K.A. Shaykhutdinov, Supercond. Sci. Technol. **21**, 085015 (2008)
12. W.H. Fietz, C. Barth, S. Drotziger, W. Goldacker, R. Heller, S.I. Schlachter, K.-P. Weiss, Fusion Eng. Des. **88**, 440 (2013)
13. Y. Ishii, T. Akasaka, Y. Kinemura, H. Ogino, S. Horii, J. Shimoyama, K. Kishio, J. Phys. Conf. Ser. **234**, 012018 (2010)
14. G.P. Mikitik, E.H. Brandt, Phys. Rev. B **64**, 184514 (2001)
15. G. Pasquini, V. Bekeris, Supercond. Sci. Technol. **19**, 671 (2006)
16. Y. Li, L. Cui, G. Cao, Q. Ma, C. Tang, Y. Wang, L. Wi, Y.Z. Zhang, Z.X. Zhao, E. Baggio-Saitovitch, Phys. C **314**, 55 (1999)
17. A. Weibel, R. Bouchet, F. Boulc'h, P. Knauth, Chem. Mater. **17**, 2378 (2005)
18. V.D. Mote, Y. Purushotham, B.N. Dole, J. Theor. Appl. Phys. **6**, 6 (2012)
19. H. Lei, K. Wang, R. Hu, H. Ryu, M. Abeykoon, E.S. Bozin, C. Petrovic, Sci. Technol. Adv. Mater. **13**, 054305 (2012)
20. H. Peng, H. Song, B. Chen, S. Lu, S. Huang, Chem. Phys. Lett. **370**, 485 (2003)
21. D.M. Gokhfeld, D.A. Balaev, M.I. Petrov, S.I. Popkov, K.A. Shaykhutdinov, V.V. Valkov, J. Appl. Phys. **109**, 033904 (2011)
22. D.M. Gokhfeld, J. Supercond. Nov. Magn. **26**, 281 (2013)
23. E. Altin, D.M. Gokhfeld, S.V. Komogortsev, S. Altin, M.E. Yakinci, J. Mater. Sci: Mater. Electron. **24**, 1341 (2013)
24. R. Lal, Phys. C **470**, 281 (2010)
25. Kh.A. Ziq, P.C. Canfield, J.E. Ostenson, D.K. Finnemore, Phys. Rev. B **60**, 3603 (1999)
26. C. Hughes, D. Dew-Hughes, Philos. Mag. **30**, 293 (1974)
27. E.J. Kramer, J. Appl. Phys. **44**, 1360 (1973)
28. V. Sandu, Mod. Phys. Lett. B **26**, 1230007 (2012)
29. M.R. Koblischka, A.J.J. van Dalen, T. Higuchi, S.I. Yoo, M. Murakami, Phys. Rev. B **58**, 2863 (1998)
30. B. Rosenstein, B.Ya. Shapiro, I. Shapiro, Y. Bruckental, A. Shaulov, Y. Yeshurun, Phys. Rev. B **72**, 144512 (2005)